

# Detection of Glaucomatous Eye via Color Fundus Images Using Fractal Dimensions

Radim KOLÁŘ, Jiří JAN

Dept. of Biomedical Engineering, Brno University of Technology, Kolejní 4, 612 00 Brno, Czech Republic

kolarr@feec.vutbr.cz

**Abstract.** This paper describes a method for glaucomatous eye detection based on fractal description, followed by classification. Two methods for fractal dimensions estimation, which give a different image/tissue description, are presented. The fundus color images are used, in which the areas with retinal nerve fibers are analyzed. The presented method shows that fractal dimensions can be used as features for retinal nerve fibers losses detection, which is a sign of glaucomatous eye.

## Keywords

Fractal, texture analysis, feature description, classification, glaucoma, retina.

## 1. Introduction

Glaucoma is the second most frequent cause of permanent blindness in industrial developed countries. It is caused by an irreversible damage of the optical nerve connected with degeneration of retinal ganglion cells, axons (neural fibers) and gliocells (providing nutrition for the axons) [18]. If not diagnosed in early stage, the damage of the optical nerve becomes permanent, which in the final stage may lead to blindness. One of the glaucoma symptoms is the gradual loss of the retinal nerve fibers (RNF), which has been proved of high diagnostic value. The RNF atrophy is indicated as a texture changes in color or grey-scale retinal photographs. Therefore, there has been a high effort to use these retinal images to evaluate a RNF since 1980 [1]. But until now, there is no routinely used method for RNF quantification (based only on color photography) although an increasing effort in this field is noticeable [2], [3], [4]. This is probably due to the expansion of new technologies in diagnosis process, mainly polarimetry [7], coherence based techniques [5], and laser reflections recording [6]. In spite of these methods, the examination by (digital) fundus camera plays a basic role in assessment of neural retinal tissue at least visually or qualitatively [23].

This paper presents new features for RNF detection, using fractal theory, applied to the texture created by RNF layer. Section 2 describes the images and their properties

with respect to RNF analysis. Section 3 shortly introduces fractal theory and its application to texture description. The results, based on the Support Vector Machine classifier are presented and discussed in Section 4. Section 5 concludes this paper.

## 2. Data

The database contained 16 color images of glaucomatous eyes with focal RNF loss and 14 color images of healthy eyes in JPEG format with very low compression. Green and blue channels were extracted from these images taken by fundus camera (Canon CF-60UDi with digital camera Canon D20). The mean value from green and blue channels was computed, because the red component doesn't carry any information from RNF layer. This is contained only on the corresponding green-blue wavelengths of reflected eye.

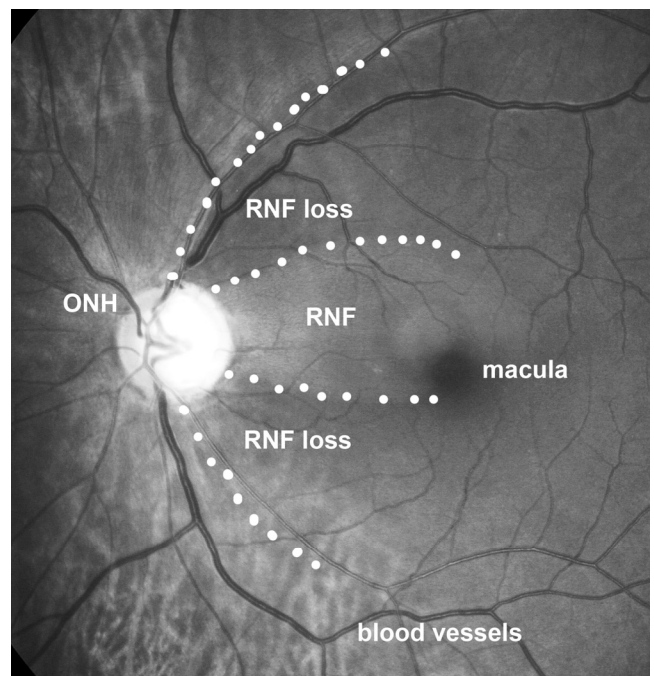


**Fig. 1.** One image from our database showing macula, optic nerve head (ONH), blood vessels and areas with/without retinal nerve fibers.

The size of the images was 3504 x 2336 pixels with a large field of view ( $60^\circ$ ). One image from that database with RNF loss is shown in Fig. 1, depicting the main structures and also two areas with RNF losses. Optical nerve head (ONH) is a place where blood vessels and RNF enters or leaves the inner eye. The macula is the place with the highest concentration of retinal ganglion cells. The RNF runs mainly from the ONH to macula with the highest concentration in radial direction (see Fig. 2 for schematic plot of retinal structures).

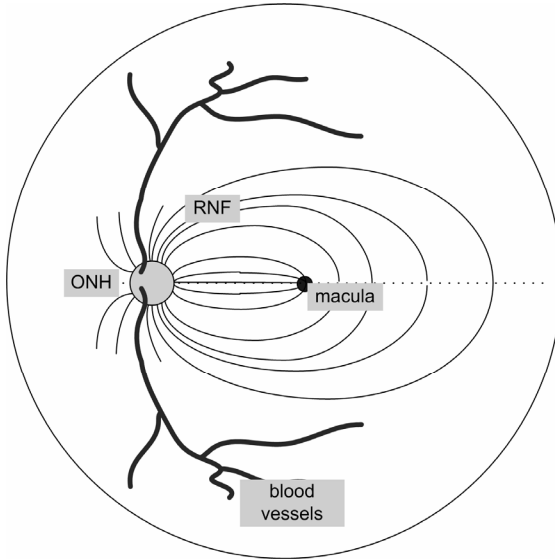


**Fig. 2.** Schematic plot of the main retinal structures. The RNF runs from the ONH to macula with the highest concentration in radial direction.

The RNF losses appear as a darker area, which is caused by a decreasing number of the nerve fiber bundles and lowering of reflection of incident light. As the reflection depends on the optical properties of the examined eye, the brightness is not a reliable feature for RNF description. Fig. 3. presents a detail of another image showing the striation RNF pattern, creating texture - the neural fibers are locally oriented in parallel, which causes their lightly stripy appearance. In the next section, the feature describing this texture based on fractal model is presented.

The testing of the new features was done on three databases of samples. The small square samples (41x41 pixels) were selected from the retinal images for texture analysis (see Fig. 3 and the black and white squares representing these samples):

- image samples with tissues containing the RNF (310 samples, class A) from patients with glaucoma (see examples depicted by the *black* squares in Fig. 3).
- image samples from area without RNF (176 samples, class B) from patients with glaucoma (see examples depicted by the *white* squares in Fig. 3).

- image samples from control group - samples selected from healthy eyes of patients without glaucoma (310 samples, class C).

The size of these samples was selected in order to span a sufficiently large region with RNF striation. The maximum size was limited by the blood vessels and other anatomical and pathological structure in the retinal image. Their positions were selected in a close surrounding around the ONH, not exceeding double radius of the ONH from ONH border. Values of pixels in all samples were normalized to the range of 1 to 256 before further processing to eliminate different illumination conditions caused by different optical eye properties.

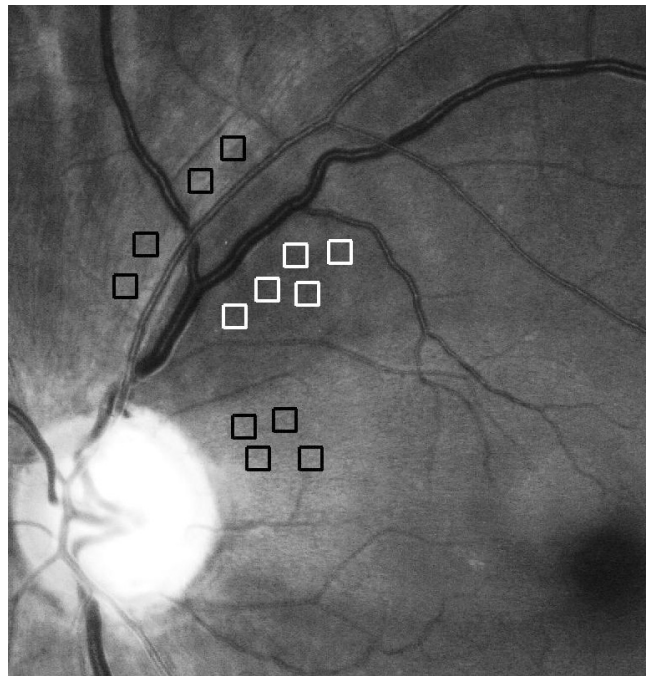


**Fig. 3.** Detail of the fundus image. The striation pattern created by RNF is visible. The dark (white) squares show the samples taken for the fractal analysis from area of RNF (loss of the RNF).

### 3. Fractal Analysis

Stochastic fractal models have been used in image processing area from late eighties [8]. Many applications can be found in the image processing research. These can be divided into two main fields: image compression using iterated function systems, e.g. [9], [10], and texture modeling connected with segmentation and usually classification. A plethora of these papers, describing fractal analysis, can be found in the medical image processing area, particularly for ultrasound images [11], [12], X-ray images [24], and magnetic resonance images [25]. Recently, only few papers can be found in the retinal image processing area [14], [15].

### 3.1 Fractal Theory

Fractals can be understood from intuitive point of view as objects with self-similarity, i.e. a considered (usually textured) object has similar characteristics repeated at different scales. One of the parameters that describes behavior of the fractal is a fractal dimension (FD), which can be considered as a measure, how complicated a particular object is (usually a curve or surface). Here, we consider self-affine fractals in one dimension, denoted by  $f(x)$ . Scaling the horizontal axis by  $r$ , the vertical axis has to be scaled as [16, p. 117]:

$$f(rx) = h(r)f(x) \quad (1)$$

where  $h(r)$  is a function of  $r$ . For stochastic process called fractional Brownian motion (fBM) holds

$$h(r) = r^H \quad (2)$$

where  $H$  is a constant characterizing fBM. Its value defines the properties of fBM process, because the absolute differences  $|f(x_1) - f(x_2)|$  have a mean value proportional to  $|x_1 - x_2|^H$ , where  $0 < H < 1$ , and  $H$  is called the Hurst exponent. The relation between  $H$  and fractal dimension is defined as [17]:

$$FD = D_T + 1 - H \quad (3)$$

where  $D_T$  is a topological dimension (1 for line, 2 for surface).

This model can be also expressed in frequency domain. If the power spectral density for function  $f(x)$  is  $P_f(\omega)$ , using the model above, we can deduce the power spectral density for  $g(x) = (1/r^H)f(rx)$  as [16, p.127]:

$$\begin{aligned} P_g(\omega) &= \frac{1}{r^{2H+D_T}} P_f\left(\frac{\omega}{r}\right) \approx \\ &\approx c_1 |\omega|^{-(2H+D_T)} = c_1 |\omega|^{-\beta_1} \end{aligned} \quad (4)$$

where the last expression holds for fBM power spectral density model [13]. From equations (3) and (4) we get:

$$FD = \frac{3D_T + 2 - \beta_1}{2}. \quad (5)$$

This equation represents a formula for FD computation, based on the estimation of spectral parameter  $\beta_1$  and topological dimension  $D_T$  (here  $D_T=2$ ).

### 3.2 Method

There are several methods for FD estimation based on different models. These methods include particularly simple box counting method, maximum likelihood estimators, and spectral-based methods. Here we present two methods based on the fBM spectral model presented in section 3.1. This model is considered in 1D and 2D, which leads to two different spectral parameters. From this point of view,

the underlying processes generate images, which can be considered as different.

The first method proposed here as a new modification for fractal dimension estimation, is based on 1D spectrum model (4). Originally, the spectrum of the image (or image sample) is two dimensional. The harmonic components of texture created by the RNF striation pattern are represented in its spectrum as an area with increased energy at spatial frequencies in the lower part of the log power spectrum. Fig. 4 shows the power spectrum obtained by periodogram method from samples of class C. This is caused by the RNF striation in different directions. On the other hand, the log power spectrum of glaucomatous eye with RNF loss (class B) has energies distributed more uniformly along the whole spectral plane as shown in Fig. 5.

These different properties can be expressed by the fractal dimension. To make the FD coefficient rotationally invariant, we propose to calculate one 1D spectrum from 2D spectrum. Consider discrete spectrum of an image sample (size  $N \times N$ ), where  $u$  and  $v$  denote indexes of spatial frequencies; one dimensional spectrum is computed:

$$P_g^{1D}(r) = \frac{1}{K} \sum_{\phi=0}^{90} P_g(u, v) \quad (6)$$

where  $u = r \cos(\phi)$  and  $v = r \sin(\phi)$ , parameter  $r$  represents the indexes for 1D frequency axis and  $K$  denotes the number of discretized angles. Spectrum  $P_g^{1D}(r)$  is the mean power spectrum profile computed from the 2D spectral plane in the first quadrant. This spectrum is modeled as 1/f process (4) and the spectral parameter  $\beta_1$  is estimated by least squares approximation of  $P_g^{1D}(r)$ . By taking logarithm of this power spectrum the linear least square fit can be used. The equation for estimation of the spectral parameter is presented below for the 2D case, which can be straightforwardly modified for this 1D case.

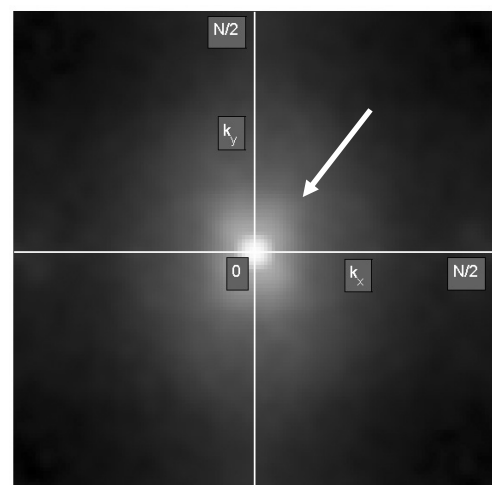


**Fig. 4.** Power spectrum obtained by periodogram method from samples from class C (healthy, control group). The white arrow indicates increased energy for image samples containing the RNF.

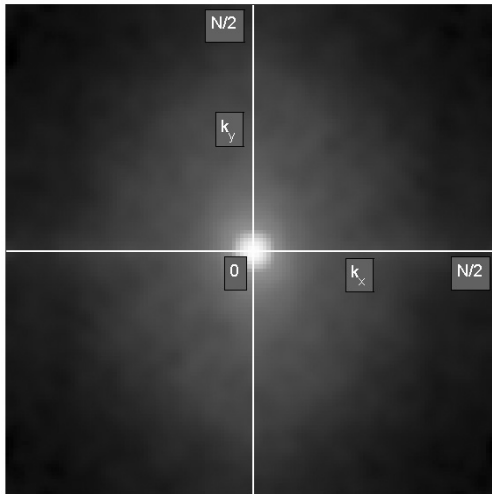


**Fig. 5.** Power spectrum obtained by periodogram method from samples from class B (samples without RNF).

The second method, described in [17], uses a direct model in 2D. For that case and for a discrete power spectrum fBM model, we can write [17]:

$$P_g^{2D}(u, v) = c_2 \cdot k_{uv}^{-\beta_2} \quad (7)$$

where  $k_{uv} = \sqrt{u^2 + v^2}$  and  $c_2$  is a constant. Using least squares approximation of the log – spectrum, parameter  $\beta_2$  can be estimated as:

$$\beta_2 = \frac{N \sum_{u,v=1}^N \ln P_g^{2D}(u, v) \ln k_{uv} - \left( \sum_{u,v=1}^N \ln k_{uv} \right) \left( \sum_{u,v=1}^N \ln P_g^{2D}(u, v) \right)}{N \sum_{u,v=1}^N (\ln k_{uv})^2 - \left( \sum_{u,v=1}^N \ln k_{uv} \right)^2}. \quad (8)$$

These two methods give estimation of the two features: fractal dimensions  $FD_1$  and  $FD_2$ , based on the spectral parameters  $\beta_1$  and  $\beta_2$ , which describe a selected image (or image sample) from two different points of view: the former as a 1D fBM process, and the latter as a 2D fBM process.

## 4. Results and Discussion

The above mentioned features ( $FD_1$  and  $FD_2$ ) were extracted from each image sample: two features were computed for all samples from each group (A, B, C). These features were used for testing the possibility of discrimination between the classes B – C and A – C, i.e. to discriminate between healthy eye (class C) and tissues from glaucomatous eye, either containing the RNF (class A) or without RNF (class B).

First, the correlation coefficient was computed for investigation the linear relationship between fractal dimensions  $FD_1$  and  $FD_2$  for classes A, B, and C. These correlation coefficients are presented in Tab. 1, showing their low linear dependency and confirming the hypothesis dealing with the difference between 1D and 2D fBm.

	Class A	Class B	Class C
$\rho_{FD1-FD2}$	0.29	0.39	0.38

**Tab. 1.** Correlation coefficients for fractal distances  $FD_1$  and  $FD_2$  within the classes.

The support vector machine (SVM) [19], [20] with soft margins (sc.  $\nu$ -SVM) was used as a classifier. This modification of classical SVM allows introducing a noise in the data, which enables overlapping between classes. The parameters of SVM were selected as follows: the Gaussian radial bases function as a kernel function with parameter 0.5 and parameter  $\nu = 0.5$ .

Two tests were conducted using LIBSVM tool [22]:

- **Test 1** – 200 samples were used for training and 100 samples for testing from the same set. This test evaluates the best classification result we are able to achieve with the selected data. Training and testing sequence was run 100 times for different sets (randomly selected) to evaluate the dependency of SVM algorithm on the training set.
- **Test 2** – a *leave-one-out* cross validation test was conducted [19]. All samples from tested groups were used for training, except one sample that was used for testing.

The results are presented in Tab. 2. The classification accuracies for samples of the RNF losses (B) with respect to samples of healthy eyes (C) are over 93%. This represents the probability with which we are able to determine the glaucomatous eye based on RNF loss analysis. In some cases the RNF losses are not so clearly visible and their (manual or automatic) segmentation can be difficult. In these cases we compare the samples of RNF of glaucomatous eye with a control group. The classification accuracy is lower (slightly over 74%), because the RNF striation is still present as in healthy eyes, but with noticeable changes.

	Test 1	Test 2
B – C	Accuracy = $93.1 \pm 2.3$ %	Accuracy = 93.8 %
	FN = $3.9 \pm 1.8$ %	FN = 4.5 %
	FP = $3.0 \pm 1.7$ %	FP = 1.7 %
A – C	Accuracy = $74.1 \pm 4.4$ %	Accuracy = 74.9 %
	FN = $11.6 \pm 3.3$ %	FN = 12.7 %
	FP = $14.3 \pm 3.2$ %	FP = 12.2 %

**Tab.2.** Results of Test 1 and Test 2 for class combination B – C and A – C.

Fig. 6 shows a plot of 2D feature space where the clusters for class B and C are obvious with a small overlap caused by ‘noise’ in the input data. This noise is introduced by small blood vessels, which impinge into the image samples and also due to JPEG artifacts. As a noise, from this point of view, the distance of samples from optic nerve head can be considered as well. Although the samples were selected in a close surrounding around

the optic nerve head, the spontaneous decrease of RNF striation with this distance influences feature's values.

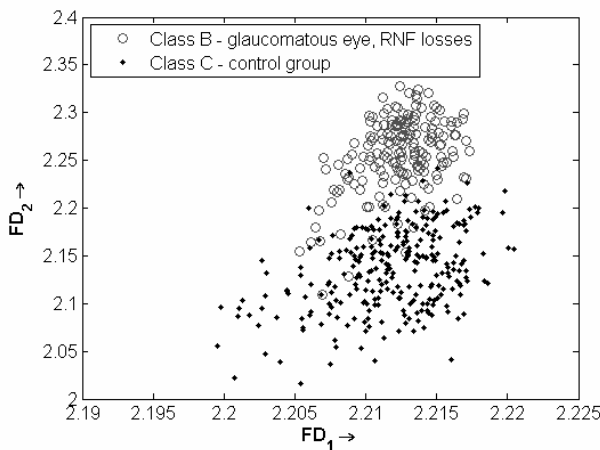


**Fig. 6.** 2D feature space FD<sub>1</sub> and FD<sub>2</sub>: features for class B and C creates clusters with a small overlap.

Fig. 7 shows the same feature space for class A and C, which introduces a large overlap of these classes, caused by RNF striation in samples for both classes. This striation is less visible in glaucomatous RNF texture.

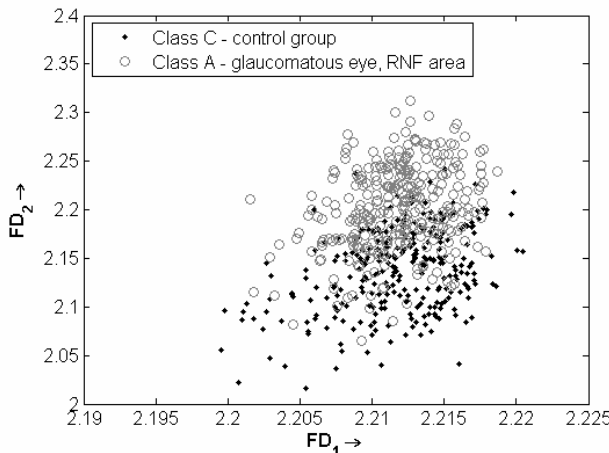


**Fig. 7.** 2D feature space FD<sub>1</sub> and FD<sub>2</sub>: features for class A and C creates clusters with a higher overlap due to RNF striation pattern in both classes.

## 5. Conclusion

Results of this approach indicate that the fractal coefficients can be used for glaucomatous eye detection in connection with the machine learning approach. This approach can be viewed as a spectral based method, using specific parameters as features. This method is computationally undemanding, which makes it convenient for clinical usage.

The accuracies for class B and C are sufficiently high showing that the proposed features may be used as a part of feature vector in Glaucoma Risk Index, as described in [26]. These features can be also used in the screening

program together with other features, based on different texture analysis methods [21], [27] and uses large database of healthy eyes as a control (reference) group.

## Acknowledgements

This work has been supported by the DAR - research center no. 1M679855501 coordinated by the Institute of Information Theory and Automation of the Czech Academy Science, and partly also by the institutional research frame no. MSM 0021630513, both grants sponsored by the Ministry of Education of the Czech Republic. The authors highly acknowledge providing the test set of images by Eye Clinic of MUDr. Kubena in Zlin (Czech Republic).

## References

- [1] PELI, E., HEDGES, T. R., SCHWARTZ, B. Computer measurement of the retina nerve fiber layer striations. *Applied Optics*, 1989, no. 28, p. 1128 - 1134.
- [2] LEE, S. Y., KIM, K. K., SEO, J. M., KIM, D. M., CHUNG, H., PARK, K. S., KIM, H. C. Automated quantification of retinal nerve fiber layer atrophy in fundus photograph. In *26<sup>th</sup> Annual International Conference of the IEEE IEMBS*. San Francisco (USA), 2004, vol. 1, p. 1241 - 1243.
- [3] OLIVA, A. M., RICHARDS, D., SAXON, W. Search for color-dependent nerve-fiber-layer thinning in glaucoma: A pilot study using digital imaging techniques. *ARVO meeting*, Fort Lauderdale (USA), 2007, e-Abstract 3309. [Online] cited 08-08-2008. Available at <http://www.arvo.org>.
- [4] TORNOW, R. P., LAEMMER, R., MARDIN, C. Quantitative imaging using a fundus camera. *ARVO meeting*, Fort Lauderdale (USA), 2007, e-Abstract 1206. [Online] cited 08-08-2008. Available at <http://www.arvo.org>.
- [5] BUDENZ, D. L. Reproducibility of retinal nerve fiber thickness measurements using the stratus OCT in normal and glaucomatous eyes. *Investigative Ophthalmology and Visual Science*, 2005, vol. 46, p. 2440 - 2443.
- [6] JANKNECHT, P., FUNK, J. Optic nerve head analyser and Heidelberg retina tomograph: accuracy and reproducibility of topographic measurements in a model eye and in volunteers. *British Journal of Ophthalmology*, 1994, vol. 78, p. 760 - 768.
- [7] HOFFMAN, E. M. et.al. Glaucoma detection using the GDx nerve fibre analyzer and the retinal thickness analyzer. *European Journal of Ophthalmology*, 2006, vol. 16, p. 251 - 258.
- [8] BARNELEY, M. F., DEVANEY, R. L., MANDELBROT, B. B. *The Science of Fractal Images*. New York: Springer-Verlag, 1988.
- [9] CARDINAL, J. Fast fractal compression of greyscale images. *IEEE Transaction on Image Processing*, 2001, vol. 10, no. 1, p. 159 - 164.
- [10] HARTENSTEIN, H., RUHL, M., SAUPE, D. Region-based fractal image compression. *IEEE Transactions on Image Processing*, 2000, vol. 9, no. 7, p. 1171 - 1184.
- [11] CHANG, R. F., CHEN, CH. J., HO, M. F., CHEN, D.-R., MOON, W. K. Breast ultrasound classification using fractal analysis. In *Proceedings of the Fourth IEEE Symposium on Bioinformatics and Bioengineering*. Taichung (Taiwan), 2004, pp. 100-107.
- [12] CHARALAMPIDIS, D., PASCOTTO, M., KERUT, E. K., LINDNER, J. R. Anatomy and flow in normal and ischemic

- microvasculature based on a novel temporal fractal dimension analysis algorithm using contrast enhanced ultrasound. *IEEE Transactions on Medical Imaging*, 2006, vol. 25, no. 8, p. 1079 to 1086.
- [13] PESQUET-POPESCU, B., VEHEL, J. L. Stochastic fractal models for image processing. *IEEE Signal Processing Magazine*, 2002, vol. 19, no. 5, p. 48 – 62.
- [14] CHENG, S. CH., HUANG, Y. M. A novel approach to diagnose diabetes based on the fractal characteristics of retinal images. *IEEE Transactions on Information Technology in Biomedicine*, 2003, vol. 7, no. 3, p. 163 – 170.
- [15] BERNDT-SCHREIBER, M. Fractal based approaches to morphological analysis of fundus eye images. *Advances in Soft Computing*, Springer, 2005, vol. 30, p. 477 – 484.
- [16] PETROU, M., SEVILLA, P. G. *Image processing: Dealing with Texture*. Wiley Publishing, 2006.
- [17] TURNER, M. J., BLACKLEDGE, J. M., ANDREWS, P. R. *Fractal Geometry in Digital Imaging*. Academic Press, 1998
- [18] LAEMMER, R., KOLÁŘ, R., JAN, J., MARDIN, C. Y. Impact of parapapillary autofluorescence in glaucoma – clinical aspects. In *Analysis of Biomedical Signals and Images*. Biosignal 2008, Brno (Czech Republic), CD-ROM proceedings, 2008, 5 pages. ISSN 1221-412X.
- [19] DUDA, R. O., HART, P. E., STORK, D. *Pattern Classification*, New York: John Wiley & Sons, 2000.
- [20] SCHOLKOPF, B., SMOLA, A. J. *Learning with Kernels. Support Vector Machines, Regularization, Optimization and Beyond*, Cambridge, MA: MIT Press, 2002.
- [21] KOLÁŘ, R., URBÁNEK, D., JAN, J. Texture based discrimination of normal and glaucomatous retina. In *Analysis of Biomedical Signals and Images*. Biosignal 2008, Brno (Czech Republic), CD-ROM proceedings, 5 pages, 2008. ISSN 1221-412X.
- [22] CHANG, C. H., LIN, C. J. *LIBSVM - A Library for Support Vector Machines*. URL: <<http://www.csie.ntu.edu.tw/~cjlin/libsvm>>.
- [23] TUULONEN, A. et al. Digital imaging and microtexture analysis of the nerve fibre layer. *Journal of Glaucoma*, 2000, vol. 9, p. 5 – 9.
- [24] JENNANE, R., OHLEY, W. J., MAJUMDAR, S., LEMINEUR, G. Fractal analysis of bone x-ray tomographic microscopy projections. *IEEE Transaction on Medical Imaging*, 2001, vol. 20, p. 443-449.
- [25] ZOOK, J., IFTEKHARUDDIN, K. Statistical analysis of fractal-based brain tumor detection algorithms. *Magnetic Resonance Imaging*, 2005, vol. 23 , no. 5, p. 671 – 678.
- [26] BOCK, R., MEIER, J., MICHELSON, G., NYÚL, L., G. HORNEGGER, J. Classifying glaucoma with image-based features from fundus photographs. *Lecture Notes in Computer Science*, Springer, 2007, vol. 4713, p. 355 – 365.
- [27] GAZÁREK, J., JAN, J., KOLÁŘ, R. Detection of neural fibre layer in retina images via textural analysis. In *Analysis of Biomedical Signals and Images*. Biosignal 2008, Brno (Czech Republic), CD-ROM proceedings, 7 pages, 2008. ISSN 1221-412X.

## About Authors ...

**Radim KOLÁŘ** was born in 1975. He has a M.Sc. degree (1998) in Cybernetics, Control and Measurement from the Brno University of Technology, Czech Republic. He has a Ph.D. degree (2002) in Biomedical Electronics and Biocybernetics from the Brno University of Technology, Czech Republic. Currently he is with the Department of Biomedical Engineering, Brno University of Technology, as research and teaching assistant. His research interests include image analysis in the field of retinal imaging, ultrasound imaging and general digital image and signal processing in biomedical engineering.

**Jiří JAN** was born 1941. He received his PhD degree in Radio Electronics from the University of Technology, Brno (1969) and scientific degree I from the Czech Academy of Sciences, Prague (1986). He is currently Full Professor of Electronics as well as Head at the Department of Biomedical Engineering and Coordinator of the Institute for Signal and Image Processing, Faculty of Electrical Engineering and Communication, Brno University of Technology. His research interests include digital signal and image processing, including applications in biomedical engineering.